AIAA SciTech Forum
6-10 January 2025, Orlando, FL
AIAA SCITECH 2025 Forum

10.2514/6.2025-2185

Check for updates

Linear response of transonic laminar shock buffet on the OALT25 airfoil

Hang Song*[1,2], Man Long Wong†[3], and Sanjiva K. Lele‡[1,2,3]
[1]*Center for Turbulence Research, Stanford University, Stanford, CA 94305, USA*
[2]*Department of Mechanical Engineering, Stanford University, Stanford, CA 94305, USA*
[3]*Department of Aeronautics & Astronautics, Stanford University, Stanford, CA 94305, USA*

A numerical study of a transonic flow over the OALT25 supercritical airfoil is conducted. The freestream Mach number is 0.735, the angle of attack is 4 deg, and the chord-length-based Reynolds number is 1 million. The laminar shock buffet is captured by a wall-resolved large-eddy simulation when the flow is statistically stationary. A modal analysis based on spectral proper orthogonal decomposition indicates that the flow system presents low-rank behavior dominated by shock buffet and turbulent vortex shedding. Several feedback paths are observed from the evolution of the dominant mode shapes. The linear response of the transonic shock buffet system is investigated by tracking the growth of perturbations via the linearized system. In the current work, the perturbation is impulsively induced within a short duration of time and localized in space slightly above the turbulent boundary layer near the trailing-edge on the suction side. The disturbances are tracked using both three-dimensional (3D) concurrently-evolved flow and two-dimensional (2D) spanwise-averaged frozen flow as the base states. The analysis identifies a feedback path through the boundary layer flow. It is observed that the feedback fluctuations within the boundary layer interact with the main shock from the pre-shock side via the Mach waves generated where the boundary layer transitions to turbulence and via the unsteadiness of the oblique shock associated with the movement of the laminar separation point on the suction side of the airfoil.

Downloaded by Stanford University on January 29, 2025 | http://arc.aiaa.org | DOI: 10.2514/6.2025-2185

I. Introduction

Shock buffet over an airfoil can create large-amplitude low-frequency fluctuations in aerodynamic loads and moments that may lead to strong aircraft structural vibrations, thus drastically limiting the flight envelope [1, 2]. Transonic shock buffet over airfoils has been widely studied both experimentally [3–6] and numerically [7–11].

For large-size airfoils operating under transonic conditions, the chord-length-based Reynolds number is sufficiently high so that the boundary layer becomes fully turbulent close to the leading edge. When shock buffet occurs, the phenomenon is commonly referred to as turbulent buffet. A variety of two-dimensional (2D) airfoil geometries, such as OAT15A [5], RA16SC1 [12], NACA 0012 [13], and NACA 64A204 [14], are provided as benchmarks for broad investigations. Numerical investigations based on the unsteady Reynolds-averaged Navier–Stokes (RANS) simulations [9, 14], wall-modeled large-eddy simulations (LES) [8, 15], and hybrid RANS/LES [10, 16, 17] as popular approaches have been undertaken for either low-cost parametric study or high-fidelity analysis of detailed mechanisms. A mechanism of transonic shock buffet over a supercritical airfoil with a fully separated turbulent boundary layer was proposed by Lee [18] based on signal processing from an experimental measurement. The theory suggests a feedback mechanism that the pressure disturbance generated from the shock propagates downstream within the separated flow region to the trailing edge and then creates upstream-traveling waves at the trailing edge which further disturbs the shock unsteadiness [18]. In addition, a global instability theory is formulated and justified to predict the onset of the turbulent shock buffet by Crouch et al. [19], where a modal linear stability of a set of perturbation fields about a steady-state mean flow provided by RANS was analyzed. Iwatani et al. [7] identifies two types of mechanisms that contribute to the shock buffet using resolvent analysis [20]. The study suggests that shock buffet is co-contributed to by both periodic pressure disturbance due to the variation of separated flow height near the trailing edge and upstream traveling pressure waves around the shock.

*Postdoctoral Fellow, Center for Turbulence Research, Stanford University. AIAA Member. (songhang@stanford.edu)
†Ph.D. Alumni, Dept. of Aeronautics & Astronautics, Stanford University. AIAA Member. (wongml@stanford.edu)
‡Edward C. Wells Professor, Dept. of Aeronautics & Astronautics, Dept. of Mechanical Engineering, Center for Turbulence Research, Stanford University. AIAA Associated Fellow. (lele@stanford.edu)

Copyright © 2025 by Hang Song, Man-Long Wong, Sanjiva K. Lele. Published by the American Institute of Aeronautics and Astronautics, Inc., with permission.

Recently, laminar supercritical airfoils, designed to maintain a considerably larger fraction of the natural laminar boundary layer at high Reynolds numbers, in contrast to the conventional airfoils with fully turbulent boundary layer, have gained increasing attention motivated by drag reduction for fuel-efficient aircraft design [21]. While operating in a transonic flow under buffeting conditions, the shock over a laminar supercritical airfoil is commonly located at the transitioning boundary layer. This phenomenon is commonly recognized as laminar shock buffet as opposed to turbulent shock buffet. A complete laminar shock buffet system contains shock-laminar boundary layer interactions, unsteadiness of laminar flow separation, shear-instability-induced flow transition to turbulence, turbulent vortex shedding, etc. Several 2D laminar supercritical airfoil geometries with their wind-tunnel experimental data are accessible for public research such as the OALT25 airfoil [22] designed by ONERA and the V2C airfoil [4] designed by Dassault Aviation. High-resolution LES transonic shock buffet over an OALT25 airfoil at a chord-length-based Reynolds number of 3 million were conducted by Dandois et al. [23] and the results were validated with the wind-tunnel measurements. Detailed shock and flow structures and signal processing results were reported, and the effects of the Kelvin–Helmholtz instability and the breathing of the separation bubble associated with turbulent vortex shedding were discussed in detail. Zauner and Sandham [24] investigated the laminar shock buffet at a low Reynolds number. The results show that the laminar shock buffet at a relatively low Reynolds number, 0.5 million, contains multiple unsteady shocks, and the primary oscillations of lift may be uncorrelated with the periodic shock motions. Zauner et al. [25] conducted spectral proper orthogonal decomposition (SPOD) analysis [26] of both OALT25 and V2C airfoils at transonic shock buffet conditions using the LES data and selected mode shapes were reported. Furthermore, the effects of flow structures and a scaling approach were justified at various Reynolds numbers. Song et al. [27] investigated the transonic laminar shock buffet at a moderately high Reynolds number, 1 million, using a high-resolution wall-resolved LES. Periodic formation of the second supersonic flow regime behind the main shock structure associated with periodic occurrence of post-shock expansion-wave and the terminating shock was observed. The SPOD analysis was conducted, and several feedback paths were studied at both shock buffet frequency and vortex shedding frequency.

Various observations from the numerical and experimental studies in both laminar and turbulent shock buffet support the hypothesis that the shock oscillation over the airfoil in transonic flows is self-sustained by one or more feedback mechanisms. However, precisely identifying a specific mechanism is challenging due to the interchangeable role of causality and influence. The current work is extended from Song et al. [27] to further investigate the feedback mechanisms observed from the SPOD analysis. Specifically, the linear response of the transonic laminar shock buffet system corresponding to locally supported impulsive perturbations is investigated. The analysis provides insights into the early-stage causality of the feedback mechanism by numerically probing the transonic laminar shock buffet system at the stationary state. The growth of the impulsive and spatially-localized perturbation identifies a more detailed consequence of the impact on the shock oscillation. In the following context, the physical and numerical configurations of the flow system are presented in Sec. II. Basic data analysis and SPOD analysis from the LES results are shown in Sec. III. The analysis of the linear response with a concurrently-evolving three-dimensional (3D) base-state flow is presented in Sec. IV.A, and the analysis of the linear response using spanwise-averaged 2D frozen base-state flows is presented in Sec. IV.B.

II. Problem configurations

A. Flow configurations

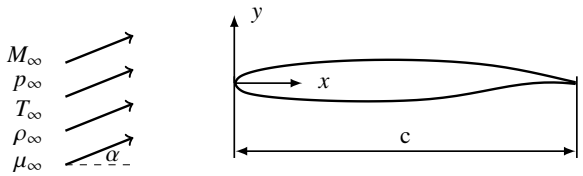

Fig. 1 Schematics of physical flow configurations [27].

The present work considers transonic flow over the OALT25 laminar supercritical airfoil with chord length c. The geometry of the airfoil is provided by ONERA [22, 23], and the schematics of the physical configurations are shown in Fig. 1. The OALT25 airfoil geometry is designed on a 2D x–y plane. In our problem setting, the chord of the airfoil is aligned with the x-direction. In 3D space, the geometry is orthogonally extruded in the spanwise (z) dimension. The

Downloaded by Stanford University on January 29, 2025 | http://arc.aiaa.org | DOI: 10.2514/6.2025-2185

freestream conditions are prescribed by the thermodynamic state, transport properties, and Mach number, M_∞. The freestream Mach number is defined as $M_\infty = U_\infty/a_\infty$ where U_∞ and a_∞ denote the flow speed (velocity magnitude) and speed of sound in the freestream respectively. Relative to the airfoil, the freestream flow is additionally prescribed by the angle of attack, α, defined as the angle between the freestream velocity vector and the vector collinear with the chord of the airfoil pointing from the leading edge (LE) to the trailing edge (TE). The chord-length-based Reynolds number, Re_c, is defined as $\mathrm{Re}_c = \rho_\infty U_\infty c/\mu_\infty$, where ρ_∞ and μ_∞ are the density and dynamic viscosity of the fluid in the freestream. The fluid is considered as a specific calorically perfect gas, and additional properties and relations are implied (cf. Sec. II.B). In this work, the freestream Mach number is $M_\infty = 0.735$, the angle of attack is $\alpha = 4°$, and the chord-length-based Reynolds number is $\mathrm{Re}_c = 1 \times 10^6$.

B. Governing equations

In this computational study, the flow is governed by the compressible Navier–Stokes equations, including conservation of mass, momentum, and total energy, shown as follows:

$$\frac{\partial \rho}{\partial t} + \frac{\partial \rho u_j}{\partial x_j} = 0 \tag{1}$$

$$\frac{\partial \rho u_i}{\partial t} + \frac{\partial}{\partial x_j}\left(\rho u_i u_j + p\delta_{ij}\right) = \frac{\partial \sigma_{ij}}{\partial x_j} \tag{2}$$

$$\frac{\partial \rho e}{\partial t} + \frac{\partial}{\partial x_j}\left(\rho h u_j\right) = \frac{\partial}{\partial x_j}\left(u_i \sigma_{ij} - q_j\right) \tag{3}$$

where the equations are expressed in the index notation, and summation convention is applied. t and x_j are the time and vector of spatial coordinate, respectively. ρ, p, e, and h are the density, pressure, specific total energy, and specific total enthalpy respectively. u_i is the velocity vector, δ_{ij} is the identity tensor, σ_{ij} is the viscous stress tensor, and q_j is the conductive heat flux. Both e and h contain a thermodynamic component and a kinematic component, $e = e_{\mathrm{th}} + u_j u_j/2$ and $h = e + p/\rho$, where e_{th} is the specific internal energy. The fluid is modeled as a calorically perfect gas specified by a specific gas constant, R, and a constant ratio of specific heats, γ. According to the equation-of-state (EOS) model of a calorically perfect gas, the internal energy only depends on the temperature, T, and is calculated as $e_{\mathrm{th}} = c_v T$ where $c_v = R/(\gamma - 1)$ is the isochoric specific heat. The relation of pressure, density, and temperature yields the ideal-gas law, $p = \rho RT$. Consistent with the EOS model of calorically perfect gas, the speed of sound, a, can be calculated as $a = \sqrt{\gamma RT}$. The viscous stress tensor is calculated based on the Newtonian-fluid constitutive relation:

$$\sigma_{ij} = 2\mu S_{ij} + \left(\beta - \frac{2}{3}\mu\right) S_{kk}\delta_{ij} \tag{4}$$

where μ and β are the dynamic shear and bulk viscosities respectively, and $S_{ij} = (u_{i,j} + u_{j,i})/2$ is the strain-rate tensor. The dynamic shear viscosity is temperature dependent and calculated based on a power-law model, $\mu = \mu_\infty (T/T_\infty)^{0.76}$, where μ_∞ and T_∞ are the dynamic shear viscosity and temperature respectively in the freestream. The dynamic bulk viscosity is calculated as $\beta = 0.67\mu$. The conductive heat flux is calculated based on Fourier's law:

$$q_j = -\kappa \frac{\partial T}{\partial x_j} \tag{5}$$

where κ is the thermal conductivity and is calculated $\kappa = c_p \mu/\mathrm{Pr}$, where Pr is the Prandtl number and treated as constant, $\mathrm{Pr} = 0.7$; and c_p is the isobaric specific heat calculated as $c_p = \gamma c_v$.

C. Configurations of the large-eddy simulation

The compressible Navier–Stokes equations are numerically solved using the wall-resolved LES approach. The Vreman subgrid-scale (SGS) model [28] and a constant turbulent Prandtl number model are applied in the momentum and total energy equations respectively. The SGS models are imposed according to the Boussinesq hypothesis. Both dynamic shear viscosity and thermal conductivity contain two components:

$$\mu = \breve{\mu} + \mu_{\mathrm{SGS}} \quad \text{and} \quad \kappa = \breve{\kappa} + \kappa_{\mathrm{SGS}}$$

where $\breve{\mu}$ and $\breve{\kappa}$ are the physically-resolved components and calculated based on the physical models described in Sec. II.B using the resolved temperature; μ_{SGS}, κ_{SGS} are the SGS components and are respectively calculated based on the Vreman

Downloaded by Stanford University on January 29, 2025 | http://arc.aiaa.org | DOI: 10.2514/6.2025-2185

SGS model [28] and a constant turbulent Prandtl number, $\mathrm{Pr}_t = 1$, as $\kappa_{\mathrm{SGS}} = c_p \mu_{\mathrm{SGS}}/\mathrm{Pr}_t$. The dynamic bulk viscosity does not have an SGS component, and it is calculated as $\beta = 0.67\breve{\mu}$.

The simulation is configured in a 3D computational domain. An O-typed body-fitted mesh is used in the x–y plane, and the mesh is uniform in the z-dimension. The size of the computational mesh is $418 \times 3072 \times 512$ in the radial, azimuthal, and spanwise dimensions respectively. The boundary conditions at the wall of the airfoil are set to be no-slip and adiabatic. A numerical sponge is applied in the far-field region to enforce the freestream conditions. The computational domain size in the spanwise dimension is $L_z = c/4$, and the domain is set to be numerically periodic in that dimension. More detailed configurations are described in Song et al. [27].

The computation is conducted primarily based on sixth-order compact finite difference methods [29]. The shock is captured by the weighted-essentially non-oscillatory interpolation scheme (WENO5-Z) [30, 31] and the approximate Riemann solver using a Rusanov flux function. The shock-capturing scheme is applied in the far-field region and is localized to the shock structures in the near-field region to compute the convective fluxes in all three directions. The shock-free flow region in the near-field region is computed by the central fluxes only. More details regarding the numerical framework and justifications of its accuracy, numerical resolution and robustness are discussed in Ref. [32] and Ref. [33], and the parallelization of the compact numerical schemes are described in Ref. [34].

Downloaded by Stanford University on January 29, 2025 | http://arc.aiaa.org | DOI: 10.2514/6.2025-2185

D. Linearized equation system

To illustrate the derivation of the linearized system, the compressible Navier–Stokes equations for the LES, Eq. (1)–Eq. (3), are denoted as

$$\frac{\partial \boldsymbol{\phi}}{\partial t} = \mathcal{F}(\boldsymbol{\phi}) \tag{6}$$

where $\boldsymbol{\phi}(\boldsymbol{x}, t)$ represents a vector of state variables, and $\mathcal{F}(\cdot)$ denotes the corresponding Navier–Stokes operator. Given a base state, $\overline{\boldsymbol{\phi}}$, the state variables can be expressed in a perturbed form by $\epsilon\boldsymbol{\phi}'(\boldsymbol{x}, t)$, as

$$\boldsymbol{\phi} = \overline{\boldsymbol{\phi}} + \epsilon\boldsymbol{\phi}' \tag{7}$$

where ϵ is a dimensionless scaling factor to keep $\|\boldsymbol{\phi}'\| / \|\boldsymbol{\phi}\| \sim O(1)$, and $\boldsymbol{\phi}'(\boldsymbol{x}, t)$ denotes the vector of scaled perturbation fields about the base state. If $\epsilon \ll 1$, the right-hand side of Eq. (6) can be written in a perturbation form about the base state $\overline{\boldsymbol{\phi}}$:

$$\frac{\partial \boldsymbol{\phi}}{\partial t} = \mathcal{F}(\overline{\boldsymbol{\phi}}) + \epsilon \mathcal{L}_{\overline{\boldsymbol{\phi}}}\boldsymbol{\phi}' + O(\epsilon^2) \tag{8}$$

where

$$\mathcal{L}_{\overline{\boldsymbol{\phi}}} = \left.\frac{\partial \mathcal{F}(\boldsymbol{\psi})}{\partial \boldsymbol{\psi}}\right|_{\boldsymbol{\psi}=\overline{\boldsymbol{\phi}}}$$

represents the Jacobian operator of $\mathcal{F}(\cdot)$ evaluated at the base state. Assuming the base state is also a solution of the LES system, the following relation is satisfied:

$$\frac{\partial \overline{\boldsymbol{\phi}}}{\partial t} = \mathcal{F}(\overline{\boldsymbol{\phi}}) \tag{9}$$

Accordingly, the system of the perturbation field is obtained from Eq. (8):

$$\frac{\partial \boldsymbol{\phi}'}{\partial t} = \mathcal{L}_{\overline{\boldsymbol{\phi}}}\boldsymbol{\phi}' + O(\epsilon) \tag{10}$$

For the perturbation fields, the Jacobian, $\mathcal{L}_{\overline{\boldsymbol{\phi}}}$, is a linear operator. If the remaining terms in $O(\epsilon)$ are truncated, Eq. (10) becomes a linearized Navier–Stokes system. For sufficiently small perturbation serving as a tracer to probe the propagation of the local flow effects, the assumption of linearized system will be valid within a certain amount of time.

According to this concept, the linearized Navier–Stokes system can be written as follows

$$\frac{\partial \rho'}{\partial t} + \frac{\partial \rho' \overline{u}_j}{\partial x_j} + \frac{\partial \overline{\rho} u'_j}{\partial x_j} = 0 \tag{11}$$

$$\frac{\partial}{\partial t}\left(\overline{\rho}u'_i + \rho'\overline{u}_i\right) + \frac{\partial}{\partial x_j}\left[\left(\rho'\overline{u}_i + \overline{\rho}u'_i\right)\overline{u}_j + p'\delta_{ij}\right] + \frac{\partial}{\partial x_j}\left(\overline{\rho}\,\overline{u}_i u'_j\right) = \frac{\partial \sigma'_{ij}}{\partial x_j} \tag{12}$$

$$\frac{\partial}{\partial t}\left(\overline{\rho}e' + \rho'\overline{e}\right) + \frac{\partial}{\partial x_j}\left[\left(\rho'\overline{h} + \overline{\rho}h'\right)\overline{u}_j\right] + \frac{\partial}{\partial x_j}\left(\overline{\rho}\,\overline{h}u'_j\right) = \frac{\partial}{\partial x_j}\left(u'_i\overline{\sigma}_{ij} + \overline{u}_i\sigma'_{ij} - q'_j\right) \tag{13}$$

where the overbar, $\overline{(\cdot)}$, and prime, $(\cdot)'$, denote the base-state and perturbation quantities respectively consistent with the definition in Eq. (7). Based on the linearized EOS model, the perturbations of pressure, p', specific total energy, e', and specific enthalpy, h', are calculated as

$$p' = R\left(\rho'\overline{T} + \overline{\rho}T'\right) \tag{14}$$

$$e' = c_v T' + \overline{u}_k u'_k \tag{15}$$

$$h' = e' + \frac{p'}{\overline{\rho}} - \left(\frac{\overline{p}}{\overline{\rho}}\right)\left(\frac{\rho'}{\overline{\rho}}\right) \tag{16}$$

σ'_{ij} and q'_j are calculated based on the linearized constitutive relations:

$$\sigma'_{ij} = 2\overline{\mu}S'_{ij} + \left(\overline{\beta} - \frac{2}{3}\overline{\mu}\right)S'_{kk}\delta_{ij} + 2\mu'\overline{S}_{ij} + \left(\beta' - \frac{2}{3}\mu'\right)\overline{S}_{kk}\delta_{ij} \tag{17}$$

$$q'_j = -\overline{\kappa}\frac{\partial T'}{\partial x_j} - \kappa'\frac{\partial \overline{T}}{\partial x_j} \tag{18}$$

In the present study, the fluctuations of the transport properties, μ', β', and κ', are not accounted for, and the simulations of the perturbation system are conducted using sixth-order compact finite differencing with WENO5-Z interpolation and the Rusanov-type approximate Riemann solver over the entire computational domain.

III. Results of the large-eddy simulation

A. Highlights of flow structures and signal processing

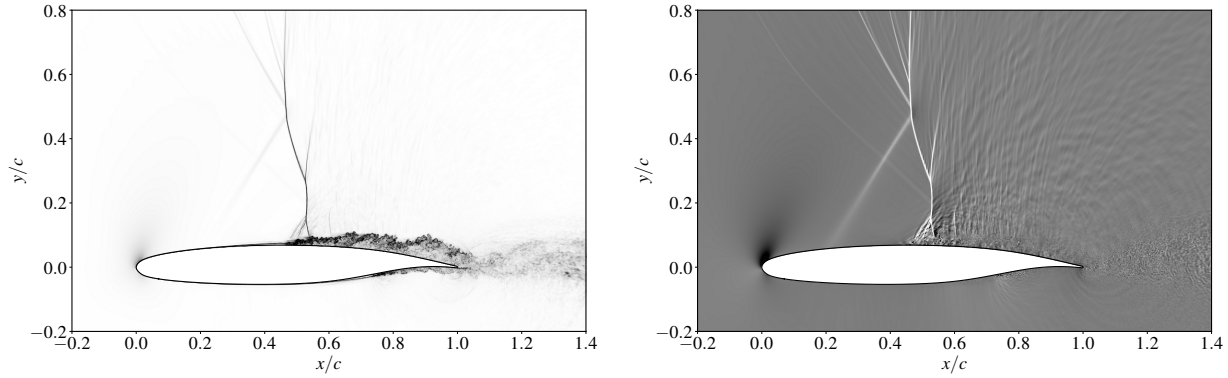

Fig. 2 Visualizations of instantaneous flow fields in an x–y cross-sectional plane at approximately 217.416 CTUs: (a) numerical Schlieren imaging ($|\nabla\rho|$) and (b) dilatation ($\nabla\cdot\vec{u}$).

After the flow reaches a statistically stationary state, data collection in the LES spans a range of approximately 260 convective time units (CTUs) at a constant time interval of approximately 2.174×10^{-2} CTUs, where the CTU is a time unit defined as c/U_∞ and can be used to non-dimensionalize the physical time as tU_∞/c. The numerical Schlieren imaging and dilatation at an instantaneous flow state are visualized in Fig. 2. Near the LE of the airfoil, the flow from a subsonic condition accelerates to a supersonic state on the suction side via an expansion wave, and the boundary layer remains laminar. As the flow continues to develop, the laminar boundary layer separates where an oblique shock is formed (which periodically becomes a strong oblique compression wave). The movement of the laminar flow separation point (described in 2D) contributes to an unsteady interaction between the oblique shock and main shock. Approximately at a distance of $0.2c$ after the laminar flow separation point, the flow transitions to turbulence due to the growth of the Kelvin–Helmholtz instability in the separated boundary layer region. The main shock foot is located above the transitioning region on the turbulent side. The transitioning turbulent boundary layer generates strong

Downloaded by Stanford University on January 29, 2025 | http://arc.aiaa.org | DOI: 10.2514/6.2025-2185

high-frequency flow fluctuations that form Mach waves and interact with the foot of the main shock. The unsteadiness of boundary layer separation and transition to turbulence form turbulent vortex shedding. At the edge of the turbulent boundary layer and extended wake region, the strong shear motion drives the turbulent flow structures to generate strong acoustic waves, and these waves radiate into the freestream region. The upstream-traveling waves get steepened as they propagate. Some of the waves directly interact with the main shock and some travel upstream over the main shock in the subsonic flow region. Such waves turn around after they pass over the shock and interact with the main shock, oblique shock, and other pre-shock flow structures. Closely behind the main shock foot, a small second supersonic flow region is periodically formed via an expansion wave, and the region ends at a terminating shock that also periodically occurs and travels towards the main shock. More details regarding this observation is described in Song et al. [27].

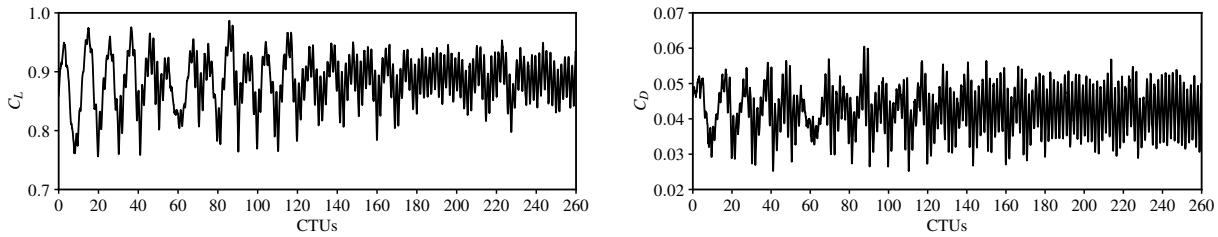

(a) (b)

Fig. 3 Time series of (a) lift coefficient, C_L, and (b) drag coefficient, C_D.

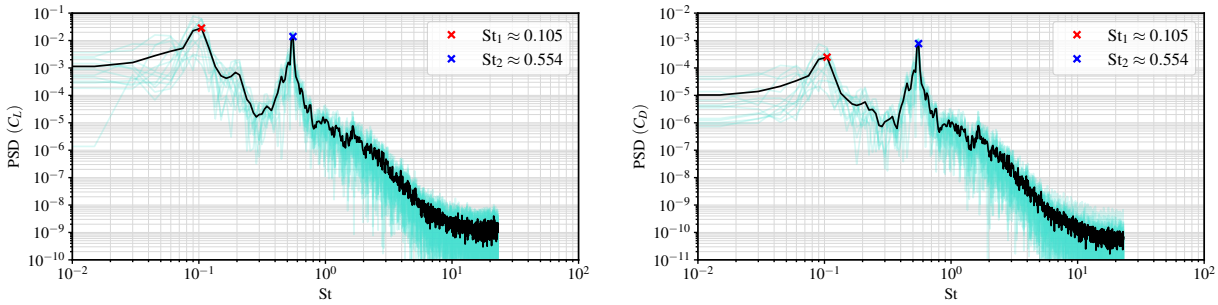

(a) (b)

Fig. 4 Power spectral densities (PSDs) of (a) lift coefficient, C_L, and (b) drag coefficient, C_D. In each plot, the black curve shows the averaged PSD using Welch's method [35], and the green curves show the PSDs obtained from each segment of consecutive data points.

In the LES, the lift coefficient, C_L, and drag coefficient, C_D, are calculated as

$$C_{L,D} = \frac{1}{A_{\text{airfoil}}} \oint_{\text{airfoil}} \left(C_f \hat{\boldsymbol{t}} - C_p \hat{\boldsymbol{n}}\right) \cdot \hat{\boldsymbol{e}}_{L,D} \, dA \tag{19}$$

where A_{airfoil} includes the 2D airfoil geometry in the x–y plane and the width in the spanwise direction; $\hat{\boldsymbol{t}}(x_w, y_w)$ is a unit vector aligned with the local tangential direction of the airfoil surface and perpendicular to the spanwise direction, where (x_w, y_w) represents a point at the airfoil surface in an x–y cross-section; $\hat{\boldsymbol{n}}(x_w, y_w)$ is a unit vector pointing to the local outgoing normal direction of the airfoil surface; $\hat{\boldsymbol{e}}_L$ and $\hat{\boldsymbol{e}}_D$ are unit vectors in the lift and drag directions, respectively; consistent with the flow configuration shown in Fig. 1, given the unit base vectors in x- and y-dimensions, $\hat{\boldsymbol{e}}_x$ and $\hat{\boldsymbol{e}}_y$, respectively, $\hat{\boldsymbol{e}}_L$ and $\hat{\boldsymbol{e}}_D$ are calculated as

$$\begin{pmatrix} \hat{\boldsymbol{e}}_L \\ \hat{\boldsymbol{e}}_D \end{pmatrix} = \begin{pmatrix} -\sin\alpha & \cos\alpha \\ \cos\alpha & \sin\alpha \end{pmatrix} \begin{pmatrix} \hat{\boldsymbol{e}}_x \\ \hat{\boldsymbol{e}}_y \end{pmatrix}$$

Downloaded by Stanford University on January 29, 2025 | http://arc.aiaa.org | DOI: 10.2514/6.2025-2185

C_f and C_p are the skin-friction coefficient and pressure coefficient evaluated locally at the airfoil surface as

$$C_f = \frac{\tau_w}{\rho U_\infty^2/2} \quad \text{and} \quad C_p = \frac{p - p_\infty}{\rho U_\infty^2/2}$$

respectively, where τ_w is the local wall shear stress, and its sign is consistent with the definition of $\hat{\boldsymbol{t}}$.

The time series of C_L and C_D are shown in Fig. 3. Associated with the buffet process, significant fluctuations in both signals of C_L and C_D are observed. Additionally, the fluctuations contain a few dominant frequencies. In the frequency domain, the power spectral densities (PSDs) of C_L and C_D are shown in Fig. 4. The frequency, f, is non-dimensionalized to the Strouhal number, St, as $\mathrm{St} = fc/U_\infty$. The PSD is calculated based on the discrete Fourier transform with the global mean of the signal removed. The sampled data are grouped into segments with 75% overlapping, and each segment contains 3072 consecutive data points. The Hann window is applied to each segment of data to avoid spectral energy leakage, and the final PSD is achieved by averaging the results obtained from each segment based on Welch's method [35]. In Fig. 4, both PSDs of C_L and C_D show two dominant frequencies at $\mathrm{St}_1 \approx 0.105$ and $\mathrm{St}_2 \approx 0.554$. The analysis provided in Song et al. [27] shows that St_1 and St_2 correspond to the shock buffet and turbulent vortex shedding, respectively. Both PSDs show sufficient decay in the high St region.

B. Data-based modal analysis using spectral proper orthogonal decomposition

The SPOD analysis [26] is conducted to investigate the space–time correlation of the flow structures in the transonic shock buffet system. The SPOD analysis formulates an eigenvalue problem:

$$\int_{\boldsymbol{x}' \in \Omega} \boldsymbol{s}(\boldsymbol{x}, \boldsymbol{x}', \mathrm{St}) \boldsymbol{w}(\boldsymbol{x}') \widehat{\boldsymbol{\psi}}(\boldsymbol{x}', \mathrm{St}) d\Omega = \lambda(\mathrm{St}) \widehat{\boldsymbol{\psi}}(\boldsymbol{x}, \mathrm{St}) \tag{20}$$

where Ω is the computational domain; $\boldsymbol{w}(\boldsymbol{x}')$ is a weighting tensor that is symmetric and positive-definite; $\lambda(\mathrm{St})$ is the eigenvalue and $\widehat{\boldsymbol{\psi}}(\boldsymbol{x}, \mathrm{St})$ is the associated SPOD eigen-mode; and $\boldsymbol{s}(\boldsymbol{x}, \boldsymbol{x}', \mathrm{St})$ is the cross-spectral density (CSD) tensor, calculated as

$$\boldsymbol{s}(\boldsymbol{x}, \boldsymbol{x}', \mathrm{St}) = \frac{1}{N} \sum_{n=1}^{N} \widehat{\boldsymbol{\phi}}_n(\boldsymbol{x}, \mathrm{St}) \widehat{\boldsymbol{\phi}}_n^*(\boldsymbol{x}', \mathrm{St}) \tag{21}$$

where N is the number of total realizations; the subscript "n" is the index for different realizations; the superscript, $(\cdot)^*$, denotes the complex conjugate in the section; and $\widehat{\boldsymbol{\phi}}_n(\boldsymbol{x}, \mathrm{St})$ is the Fourier transform of the vector of state variables $\boldsymbol{\phi}_n(\boldsymbol{x}, t)$ in time. The forms of $\boldsymbol{s}$ and $\boldsymbol{w}$ permit an orthogonal eigen-decomposition with semi-positive-definite eigenvalues. For the same St, different SPOD modes are orthogonal with consistent inner product:

$$\int_{\boldsymbol{x}' \in \Omega} \widehat{\boldsymbol{\psi}}_i^*(\boldsymbol{x}', \mathrm{St}) \boldsymbol{w}(\boldsymbol{x}') \widehat{\boldsymbol{\psi}}_j(\boldsymbol{x}', \mathrm{St}) d\Omega = \delta_{ij} \tag{22}$$

where the subscript indicates the rank of eigen-mode. In the description related to the SPOD analysis, the summation convention does not apply. The formulation of eigenvalue problem allows an expansion of the CSD tensor in terms of orthogonal eigenbasis:

$$\boldsymbol{s}(\boldsymbol{x}, \boldsymbol{x}', \mathrm{St}) = \sum_{i=1}^{N} \lambda_i(\mathrm{St}) \widehat{\boldsymbol{\psi}}_i(\boldsymbol{x}, \mathrm{St}) \widehat{\boldsymbol{\psi}}_i^*(\boldsymbol{x}', \mathrm{St}) \tag{23}$$

In discrete representation, the eigenvalue problem is formulated as

$$\frac{1}{N} \widehat{\boldsymbol{\Phi}} \widehat{\boldsymbol{\Phi}}^H \boldsymbol{W} \widehat{\boldsymbol{\Psi}} = \widehat{\boldsymbol{\Psi}} \boldsymbol{\Lambda} \tag{24}$$

where each column in $\widehat{\boldsymbol{\Phi}}$ contains a single realization of the Fourier transformed state variables that are obtained from the computational mesh, so $N^{-1} \widehat{\boldsymbol{\Phi}} \widehat{\boldsymbol{\Phi}}^H$ represents the CSD in discrete space; $\boldsymbol{W}$ becomes a block-diagonal matrix representing $\boldsymbol{w}(\boldsymbol{x}') d\Omega$; $\boldsymbol{\Lambda}$ is an $N \times N$ diagonal matrix containing all the eigenvalues; and the columns in $\widehat{\boldsymbol{\Psi}}$ are the corresponding discrete eigen-modes. For simplicity, assume the Fourier transformed variables only contain a single mode at a specific St. As described in Towne et al. [26] and Schmidt and Colonius [36], an efficient approach can be applied to solve the eigenvalue problem with significant reduction of computational cost. The cost reduction is achieved based on the assumption that the number of total realizations, N, is significantly smaller than the total number of data

Downloaded by Stanford University on January 29, 2025 | http://arc.aiaa.org | DOI: 10.2514/6.2025-2185

points in each realization. In other words, the cost reduction requires that $\widehat{\boldsymbol{\Phi}}$ is a skinny matrix. To derive the approach, left- and right- multiply by $\widehat{\boldsymbol{\Phi}}^H \boldsymbol{W}$ and $\boldsymbol{\Lambda}^{-1/2}$ respectively on each side of Eq. (24). As a result, an equivalent eigenvalue problem is formulated that does not include identically trivial eigen-modes:

$$\frac{1}{N}\left(\widehat{\boldsymbol{\Phi}}^H \boldsymbol{W} \widehat{\boldsymbol{\Phi}}\right) \widehat{\boldsymbol{\Theta}} = \widehat{\boldsymbol{\Theta}} \boldsymbol{\Lambda} \tag{25}$$

where $\widehat{\boldsymbol{\Theta}} = N^{-1/2} \widehat{\boldsymbol{\Phi}}^H \boldsymbol{W} \widehat{\boldsymbol{\Psi}} \boldsymbol{\Lambda}^{-1/2}$ is an $N \times N$ unitary matrix. In the efficient calculation, Eq. (25) is used to compute the eigenvalues, and the columns in $\widehat{\boldsymbol{\Theta}}$ corresponding to selected eigenvalues can be also computed with considerably affordable cost. The eigen-modes corresponding to the selected eigenvalues can be calculated as

$$\widehat{\boldsymbol{\Psi}} = \frac{1}{\sqrt{N}} \widehat{\boldsymbol{\Phi}} \widehat{\boldsymbol{\Theta}} \boldsymbol{\Lambda}^{-1/2} \tag{26}$$

where $\widehat{\boldsymbol{\Theta}}$ and $\boldsymbol{\Lambda}$ do not have to be at the full size of $N \times N$. $\widehat{\boldsymbol{\Theta}}$ may only contain columns corresponding to the selected eigenvalues stored in the reduced diagonal entries of $\boldsymbol{\Lambda}$. The result of $\widehat{\boldsymbol{\Psi}}$ calculated from Eq. (26) guarantees the discrete orthogonality equivalent to Eq. (22):

$$\widehat{\boldsymbol{\Psi}}^H \boldsymbol{W} \widehat{\boldsymbol{\Psi}} = \boldsymbol{I} \tag{27}$$

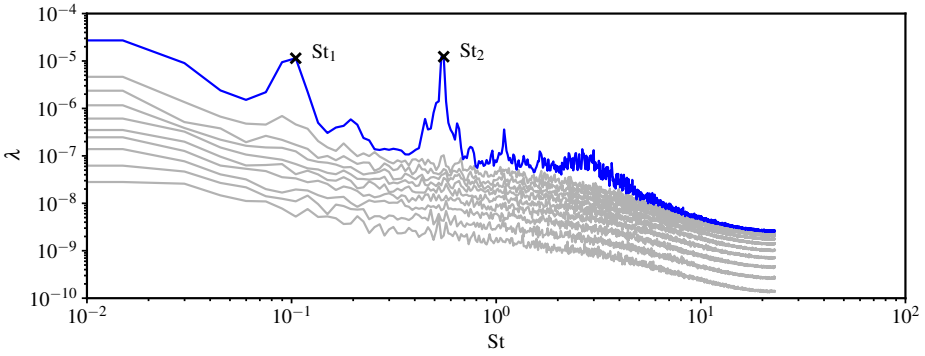

Fig. 5 Spectra of the ten largest eigenvalues in the SPOD analysis using the Chu norm [37]. The marked frequencies are $\mathrm{St}_1 \approx 0.105$ and $\mathrm{St}_2 \approx 0.554$, respectively.

The Chu norm is used to characterize the fluctuating energy in compressible flow [37]. In this work, the Chu norm, E_{Chu}, can be generally expressed as

$$E_{\mathrm{Chu}} = \frac{1}{L_z} \int_{\boldsymbol{x} \in \Omega} \varepsilon(\boldsymbol{x}, t) d\Omega \tag{28}$$

where

$$\varepsilon = \frac{1}{2}\left(\overline{\rho} u_k' u_k' + \frac{\overline{a}^2}{\gamma \overline{\rho}} \rho'^2 + \frac{\overline{\rho} c_v}{\overline{T}} T'^2\right) \tag{29}$$

According to the definitions in Eq. (28) and Eq. (29), the physical units of ε and E_{Chu} are "energy per unit volume" and "energy per unit width of span," respectively. The definitions of E_{Chu} and ε in Eq. (28) and Eq. (29) are used in both the SPOD analysis in this section and the analysis of linear response discussed in Sec. IV. The definitions of overbar, $\overline{(\cdot)}$, and prime, $(\cdot)'$, are consistent with the decomposition in Eq. (7) as the base state and perturbation, respectively. For different analysis, the definitions of "base state" and "perturbation" are specific. In the SPOD analysis, the overbar indicates that a quantity is averaged in time, and the prime represents the local temporal fluctuation correspondingly. Consistent with the definitions of E_{Chu} and ε, the weighting tensor is

$$\boldsymbol{w}(\boldsymbol{x}) = \frac{1}{2}\mathrm{diag}\left(\overline{\rho},\ \overline{\rho},\ \overline{\rho},\ \frac{\overline{a}^2}{\gamma \overline{\rho}},\ \frac{\overline{\rho} c_v}{\overline{T}}\right) \tag{30}$$

where the five diagonal entries correspond to the three components of the velocity vector, u_i', density, ρ', and temperature, T', respectively. The discrete Fourier transform at each grid point of the computational mesh is conducted in the same

Downloaded by Stanford University on January 29, 2025 | http://arc.aiaa.org | DOI: 10.2514/6.2025-2185

setup as stated in Sec. III.A. The SPOD analysis is conducted in an x–y cross-sectional plane. Correspondingly, L_z is set to unity and $d\Omega$ degenerates to characteristic local mesh area in the x–y plane consistent with the computational mesh used in the LES.

The spectra of the ten largest eigenvalues are shown in Fig. 5. The spectrum of the largest eigenvalue peaks at $\mathrm{St} \approx 0.105$ and $\mathrm{St} \approx 0.554$ which are equal to St_1 and St_2 identified in the PSDs of C_L and C_D as shown in Fig. 4. St_1 and St_2 correspond to the St of shock buffet and turbulent vortex shedding, respectively. Compared to the spectrum of the second-largest eigenvalue in Fig. 5, at St_1 and St_2, the first eigenvalue is larger than the rest of the eigenvalues by orders of magnitude. Combined with the eigen-expansion of the CSD tensor in Eq. (23), this behavior, from the perspective of space–time correlation, indicates that the flow structures have low-rank representation at each of the peak frequencies.

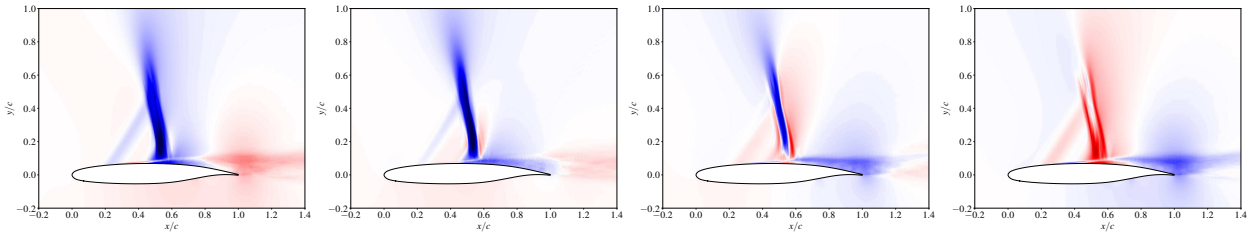

(a) (b) (c) (d)

Fig. 6 Evolution of the density fluctuations corresponding to the first SPOD mode at the shock buffet frequency, $\mathrm{St}_1 \approx 0.105$: (a) $\varphi = 0$, (b) $\varphi = \pi/4$, (c) $\varphi = \pi/2$, (d) $\varphi = 3\pi/4$, where $\varphi \in [0, 2\pi)$ is the phase angle.

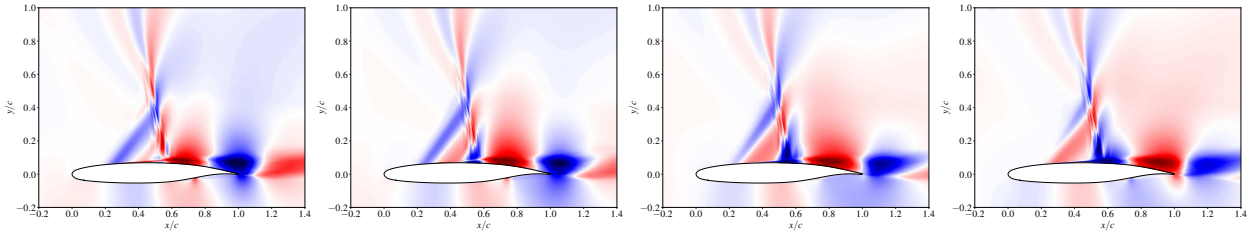

(a) (b) (c) (d)

Fig. 7 Evolution of the density fluctuations corresponding to the first SPOD mode at the vortex shedding frequency, $\mathrm{St}_2 \approx 0.554$: (a) $\varphi = 0$, (b) $\varphi = \pi/4$, (c) $\varphi = \pi/2$, (d) $\varphi = 3\pi/4$, where $\varphi \in [0, 2\pi)$ is the phase angle.

The low-rank coherent flow structures at a specified St are represented by the SPOD mode with respect to the first eigenvalue. The evolution of the SPOD mode is denoted as

$$\boldsymbol{\psi}(\boldsymbol{x}, \varphi, \mathrm{St}) = \widehat{\boldsymbol{\psi}}(\boldsymbol{x}, \mathrm{St}) e^{i\varphi} \tag{31}$$

where $\boldsymbol{\psi}(\boldsymbol{x}, \varphi, \mathrm{St})$ is the SPOD mode shown in physical space, and φ is a phase angle. For a specific St, the phase angle is calculated as $\varphi(t, \mathrm{St}) = 2\pi \mathrm{St}(tU_\infty/c)$. The low-rank coherent density fluctuations, corresponding to the real component of $\boldsymbol{\psi}(\boldsymbol{x}, \varphi, \mathrm{St})$, at the shock buffet ($\mathrm{St}_1 \approx 0.105$) and turbulent vortex shedding ($\mathrm{St}_2 \approx 0.554$) Strouhal numbers are shown in Fig. 6 and Fig. 7, respectively. The reconstructed low-rank fluctuating density fields at each St capture the main flow structures including the main shock, oblique shock, boundary layer, and wake flows. Additionally, detailed flow structures on the suction side of the airfoil, such as the laminar boundary layer separation, thin shear layer growth, periodic formation of separation bubble and shedding vortices, and acoustic radiation in the freestream are also clearly captured. Specifically, the evolution of density fluctuations at St_1 (Fig. 6) shows the low-frequency boundary layer breathing at large scale. At St_2 (Fig. 7), the first density mode captures the shedding vortices by the non-radiative pseudo-sound structures. Three major feedback paths are identified from the evolution of the first SPOD modes at both St_1 and St_2. The fluctuations in the downstream region behind the main shock propagate towards upstream direction and reach the pre-shock flow region. One path is via the region above the main shock, and another path is on the

Downloaded by Stanford University on January 29, 2025 | http://arc.aiaa.org | DOI: 10.2514/6.2025-2185

pressure side of the airfoil. These two paths primarily carry the acoustic energy generated by the turbulent boundary layer/shedding vortices and via TE acoustic scattering. Moreover, the path in the boundary layer for fluctuations propagating upstream below the main shock foot is believed to play an important role in the feedback mechanism. Via this path, the post-shock fluctuations travel upstream through the boundary layer bypassing the main shock, and the fluctuations rejoin the near-field freestream by radiating Mach waves. These Mach waves can directly interact with the main shock in the lower portion. The unsteadiness of the laminar boundary layer separation point (described based on a 2D view) resulting from the feedback disturbance causes fluctuations of the oblique shock. Since the flow across the oblique shock remains supersonic, the fluctuation will also impact the interaction between the oblique shock and the main shock. The explanation of the feedback mechanism via this path is supported by the visualizations of the LES results and SPOD mode shapes, especially those evolving in the triangular flow region surrounded by the oblique shock, main shock, and airfoil surface. Additionally, the observations in this work are also consistent with the observations and conclusions from related studies in Iwatani et al. [7] and Zauner et al. [25] on resolvent analysis of turbulent shock buffet and laminar shock buffet at different Reynolds numbers, respectively.

Downloaded by Stanford University on January 29, 2025 | http://arc.aiaa.org | DOI: 10.2514/6.2025-2185

IV. Analysis of transient linear response

The linearized system in Sec. II.D is homogeneous. An initial perturbation is needed to activate the non-trivial evolution of the perturbation fields. In this work, the initial perturbation is introduced to the system by a pseudo body force. The force is impulsive with short duration, localized in the x–y plane, and uniform in the spanwise dimension. The expression for the pseudo body force is

$$b_i' = A_f \left(\frac{U_\infty^2}{c}\right) \left(\frac{t}{\Delta t_f}\right)^2 \exp\left[1 - \left(\frac{t}{\Delta t_f}\right)^2 - \left(\frac{r}{r_f}\right)^2\right] \delta_{i2} \tag{32}$$

where A_f is a dimensionless amplitude; Δt_f is a characteristic duration serving as a time scale; r_f is a characteristic radius of the forcing region; r is the distance away from the center location of the forcing region; given the center coordinate, (x_f, y_f), r is calculated as $r = \sqrt{(x - x_f)^2 + (y - y_f)^2}$; δ_{i2} indicates that the forcing is only applied along the positive y-direction. To the right-hand side of the linearized momentum equation, Eq. (12), the pseudo body force is added as $\overline{\rho} b_i'$. Consistently, the pseudo work, $\overline{\rho} b_j' \overline{u}_j$, is added to the right-hand side of the linearized energy equation, Eq. (13). Since the linearized system is homogeneous other than the impulsive forcing, the forcing amplitude A_f does not affect the normalized solution. In this work, the center location of the forcing region is $x_f/c = 0.85$ and $y_f/c = 0.05$, the characteristic duration is $\Delta t_f U_\infty/c = 0.002$, and the characteristic radius is $r_f/c = 0.00375$. The forcing is located slightly above the turbulent boundary layer on the suction side near the TE. The exact forcing location relative to the airfoil and its amplitude variation in time are shown in Fig. 8.

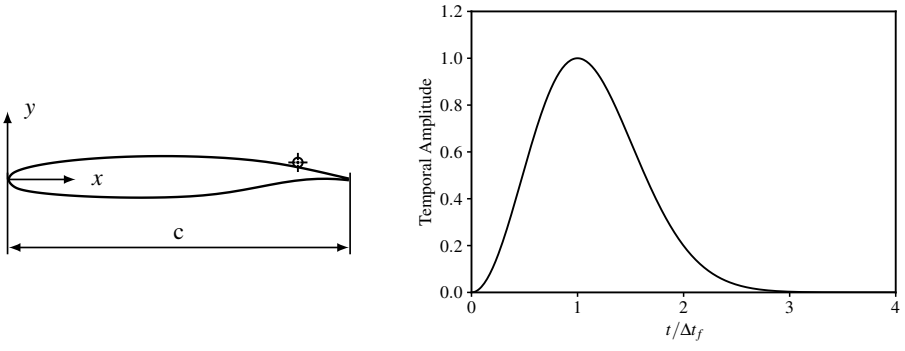

Fig. 8 Schematic of initial perturbation: (a) center location marked by "⌖" at $(0.85c, 0.05c)$ and (b) evolution of the center-point perturbation amplitude, where the characteristic duration is $\Delta t_f U_\infty/c = 0.002$.

The growth of the perturbation is tracked for two different types of base states. In Sec. IV.A, the linear response of the buffet system corresponding to a concurrently-evolving base state is discussed. Furthermore, the linear responses corresponding to several frozen base states are also discussed in Sec. IV.B.

A. Linear response of a 3D concurrently-evolving base-state flow

The results presented in this subsection correspond to a concurrently-evolving base state. The base state is one-way coupled to the evolution of the perturbation fields but is not affected by the growth of perturbation. During the simulation of the linearized system, the base state is concurrently solved by the LES solver, and the synchronized results from the LES at the same computational time are passed to the linearized system during the runtime. In this context, the base state variables are considered to be functions of both space and time, $\bar{\boldsymbol{\phi}}(\boldsymbol{x}, t)$. The simulation starts from the LES solution at the 217.416 CTUs. The base state is the same as visualized in Fig. 2. For the simulation of the linearized system, the computational time is reset to zero. Accordingly, $tU_\infty/c = 0$ corresponds to the starting point of the simulation of the linearized system. This definition is consistent with the time variable used in Eq. (32). The absolute energy of the linear response of the system is quantified by the Chu norm [37], $E_{\text{Chu}}(t)$. The definition is consistent with the expressions in Eq. (28) and Eq. (29).

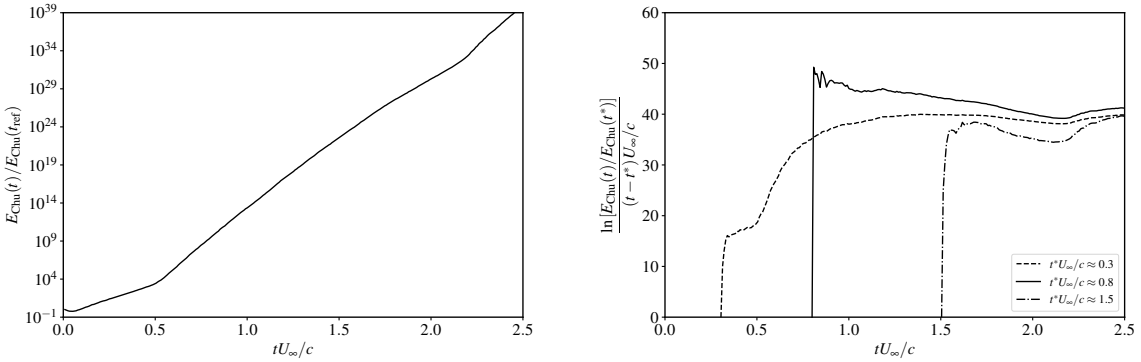

(a) (b)

Fig. 9 Growth of the perturbation amplitude about a concurrently-evolving base state measured by the Chu norm [37]: (a) time history of the perturbation amplitude and (b) estimation of the rate of linear growth at different measurement times, t^*.

The relative energy of the total linear response over the entire computational domain is characterized by the quantity $E_{\text{Chu}}(t)/E_{\text{Chu}}(t_{\text{ref}})$, and the growth of the relative energy is shown in Fig. 9a. The form of the pseudo body force, Eq. (32), used in this work, is consistent with $E_{\text{Chu}}/(\rho U_\infty^2 c^2) = 0$ at $t = 0$. For a valid normalization, $E_{\text{Chu}}(t_{\text{ref}})$ is used for scaling where $t_{\text{ref}}U_\infty/c \approx 0.00217$. As shown in Fig. 9a, after a short adjustment, E_{Chu} approximately shows a linear growth (with a constant growth rate) for $tU_\infty/c < 0.5$. After $tU_\infty/c \approx 0.5$, the growth rate increases, but E_{Chu} still approximately shows a different linear growth. Within 2.5 CTUs, the total linear response, indicated by E_{Chu}, significantly increases by many orders of magnitude.

The local growth rate can be measured at a given time, t^*. Assuming a model growth near $t = t^*$, E_{Chu} has the following asymptotic behavior, $E_{\text{Chu}}(t) \sim e^{\sigma(t-t^*)U_\infty/c}$, where $\sigma(t^*)$ is a local non-dimensional growth rate. The calculation of σ at a given t^* can be analytically expressed as

$$\sigma(t^*) = \left.\frac{d \ln\left[E_{\text{Chu}}(t)/E_{\text{Chu}}(t_{\text{ref}})\right]}{d(tU_\infty/c)}\right|_{t=t^*} \tag{33}$$

For $t > t^*$ and $(t - t^*)U_\infty/c \ll 1$, σ can be approximated as

$$\sigma(t^*) = \lim_{t \to t^{*+}} \frac{\ln\left[E_{\text{Chu}}(t)/E_{\text{Chu}}(t^*)\right]}{(t - t^*)U_\infty/c} \tag{34}$$

According to this approach, σ is measured at different values of t^*U_∞/c of approximately 0.3, 0.8, and 1.5 respectively, and the results are shown in Fig. 9b. According to the measurements, the values of σ corresponding to the three different $t^*U_\infty/$ are approximately 16, 48, and 37, respectively.

At different stages, the power density of the Chu norm, $\varepsilon(\boldsymbol{x}, t)$, and the density fluctuation, $\rho'(\boldsymbol{x}, t)$, are visualized in Fig. 10 and Fig. 11, respectively. The visualizations focus on showing the structures of the linear response corresponding to the initial perturbation. Therefore, the fields of $\varepsilon(\boldsymbol{x}, t)$ and $\rho'(\boldsymbol{x}, t)$ are dynamically scaled by $\varepsilon_{\text{ref}}(t)$ and $\rho'_{\text{ref}}(t)$,

Downloaded by Stanford University on January 29, 2025 | http://arc.aiaa.org | DOI: 10.2514/6.2025-2185

respectively. In this work, the scaling quantities are:

$$\varepsilon_{\text{ref}}(t) = \frac{1}{L_z c^2} \int_{x\in\Omega} \varepsilon(\boldsymbol{x}, t) d\Omega \quad \text{and} \quad \rho'_{\text{ref}}(t) = \left[\frac{1}{L_z c^2} \int_{x\in\Omega} \rho'^2(\boldsymbol{x}, t) d\Omega \right]^{1/2}$$

Furthermore, an additional power law is applied for a better visualization quality. The power law for each visualization is stated in the captions of Fig. 10 and Fig. 11.

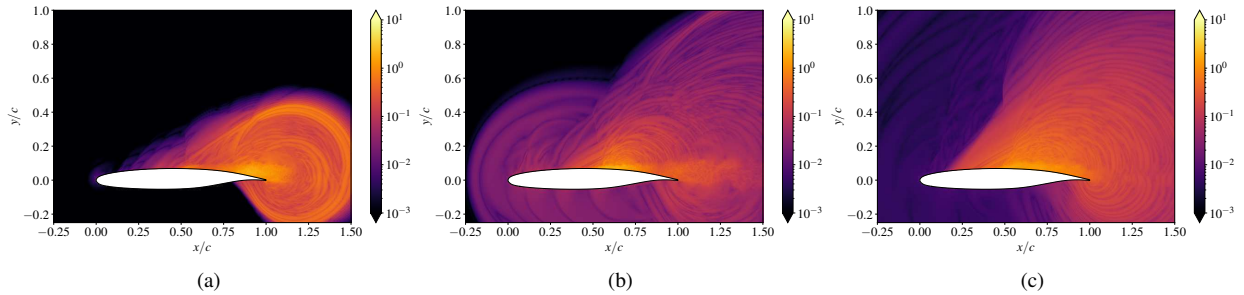

(a) (b) (c)

Fig. 10 Visualization of the instantaneous Chu-norm power density of the linear response, $(\varepsilon(x,t)/\varepsilon_{\text{ref}}(t))^{1/m}$: (a) $tU_\infty/c \approx 0.30$ and $m = 7$; (b) $tU_\infty/c \approx 0.80$ and $m = 7$; (c) $tU_\infty/c \approx 1.50$ and $m = 11$.

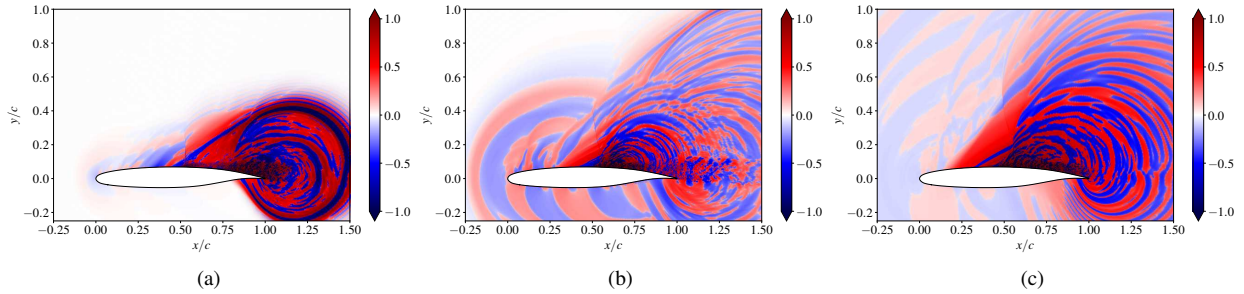

(a) (b) (c)

Fig. 11 Visualization of instantaneous density fluctuations in the linear response, $\left(\rho'/\rho'_{\text{ref}}\right)^{1/m}$: (a) $tU_\infty/c \approx 0.30$ and $m = 7$; (b) $tU_\infty/c \approx 0.80$ and $m = 7$; (c) $tU_\infty/c \approx 1.50$ and $m = 11$.

The visualizations in Fig. 10 and Fig. 11 show that the initial perturbation grows in both upstream and downstream directions. The downstream-traveling perturbations are scattered at the TE, and the scattering generates upstream-traveling perturbations on the pressure side of the airfoil. The upstream-traveling perturbations on the suction side of the airfoil become steepened in the near-field freestream and are blocked by the main shock (in the base state). In contrast, the perturbations within the boundary layer bypass the main shock below the shock foot and reach the pre-shock flow region. These perturbations then propagate to the freestream and radiate into the main shock region. Further upstream-traveling perturbations on the suction side propagate to the freestream near the LE, and some of the perturbations reach the pressure side and keep traveling downstream. The structures of the linear response on the pressure side of the airfoil are formed due to the interaction between the upstream- and downstream-traveling perturbations from the TE and LE, respectively.

B. Linear response of 2D spanwise-averaged frozen base-state flows

The linear response corresponding to a frozen base-state is also investigated. The base state flow is created by conducting spanwise averaging of an instantaneous LES solution. The density field is averaged, consistent with Reynolds averaging. The velocity and temperature are calculated by density-weighted averaging, which is consistent with Favre average. Despite the spanwise averaging, the 2D base state still well captures the instantaneous large-scale flow structures in the x–y plane, such as the main shock, oblique shock, laminar boundary layer, and vortex shedding. The simulation of the linearized system is conducted in 2D. During the time advancement, only perturbation fields are updated.

Downloaded by Stanford University on January 29, 2025 | http://arc.aiaa.org | DOI: 10.2514/6.2025-2185

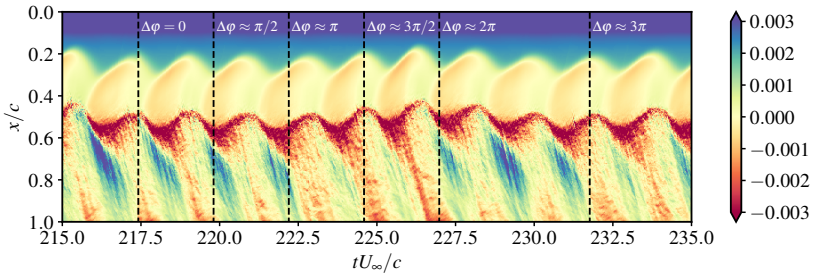

Fig. 12 x–t diagram of spanwise-averaged skin-friction coefficient (C_f) on the suction side. The phase angles ($\Delta\varphi$) for selected frozen base states are marked. The phase angles are calculated based on the shock-buffet frequency at $St_1 \approx 0.105$.

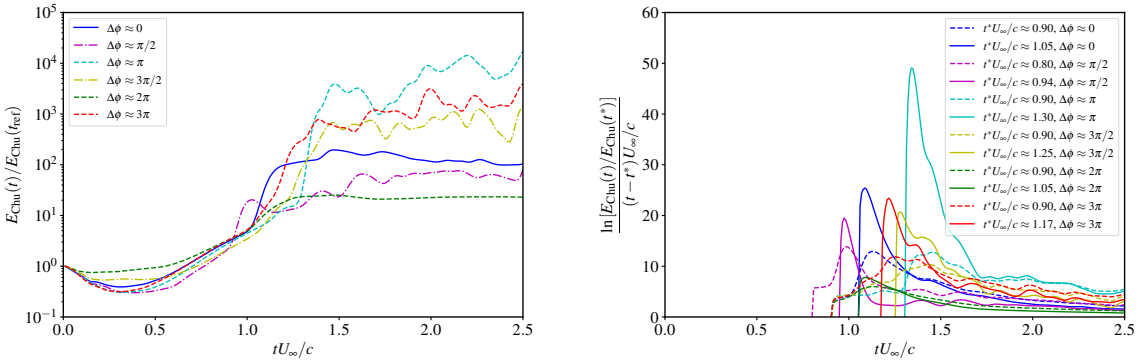

(a) (b)

Fig. 13 Growth of the perturbation amplitude about a frozen base state measured by the Chu norm [37]: (a) time history of the perturbation amplitude and (b) estimation of the rate of linear growth at different measurement times, t^*.

According to the illustrations in Sec. II.D, a frozen base state has the form $\overline{\boldsymbol{\phi}}(\boldsymbol{x})$ which does not vary with time. However, a frozen base state is not guaranteed to satisfy the original system, viz. $\mathcal{F}(\overline{\boldsymbol{\phi}}) \neq \mathbf{0}$ for arbitrary $\overline{\boldsymbol{\phi}}$, because such frozen base state may not be a steady-state solution to the original system. Therefore, enforcing a frozen base state implies a source term added to the original dynamic system. The modified dynamic system that allows a frozen base state can be expressed as

$$\frac{\partial \boldsymbol{\phi}}{\partial t} = \mathcal{F}(\boldsymbol{\phi}) - \mathcal{F}(\overline{\boldsymbol{\phi}}) \tag{35}$$

where the term $-\mathcal{F}(\overline{\boldsymbol{\phi}})$ artificially enforces an equilibrium point at the specified base state, and since the base state is frozen, this term is time-independent. Consistent with the decomposition defined in Eq. (7), Eq. (35) can be written in terms of $\boldsymbol{\phi}'$ and $\overline{\boldsymbol{\phi}}$:

$$\epsilon \frac{\partial \boldsymbol{\phi}'}{\partial t} = \mathcal{F}\left(\overline{\boldsymbol{\phi}} + \epsilon \overline{\boldsymbol{\phi}}'\right) - \mathcal{F}(\overline{\boldsymbol{\phi}}) \tag{36}$$

Assuming $\epsilon \ll 1$, the first term on the right-hand side of Eq. (36) can be written in the form of a Taylor series expansion. It can be observed that the leading-order term of the Taylor series expansion balances the implied source term, and the perturbation system becomes:

$$\frac{\partial \boldsymbol{\phi}'}{\partial t} = \mathcal{L}_{\overline{\boldsymbol{\phi}}}(\boldsymbol{\phi}') + O(\epsilon)$$

where the form of the equation is identical to Eq. (10). The resulting linearized system does not contain any forcing or source terms after imposing the initial perturbation. The evolutions of perturbation fields only depend on the choice of the base state. For slowly varying flow structures corresponding to the low-frequency flow features, using an averaged

Downloaded by Stanford University on January 29, 2025 | http://arc.aiaa.org | DOI: 10.2514/6.2025-2185

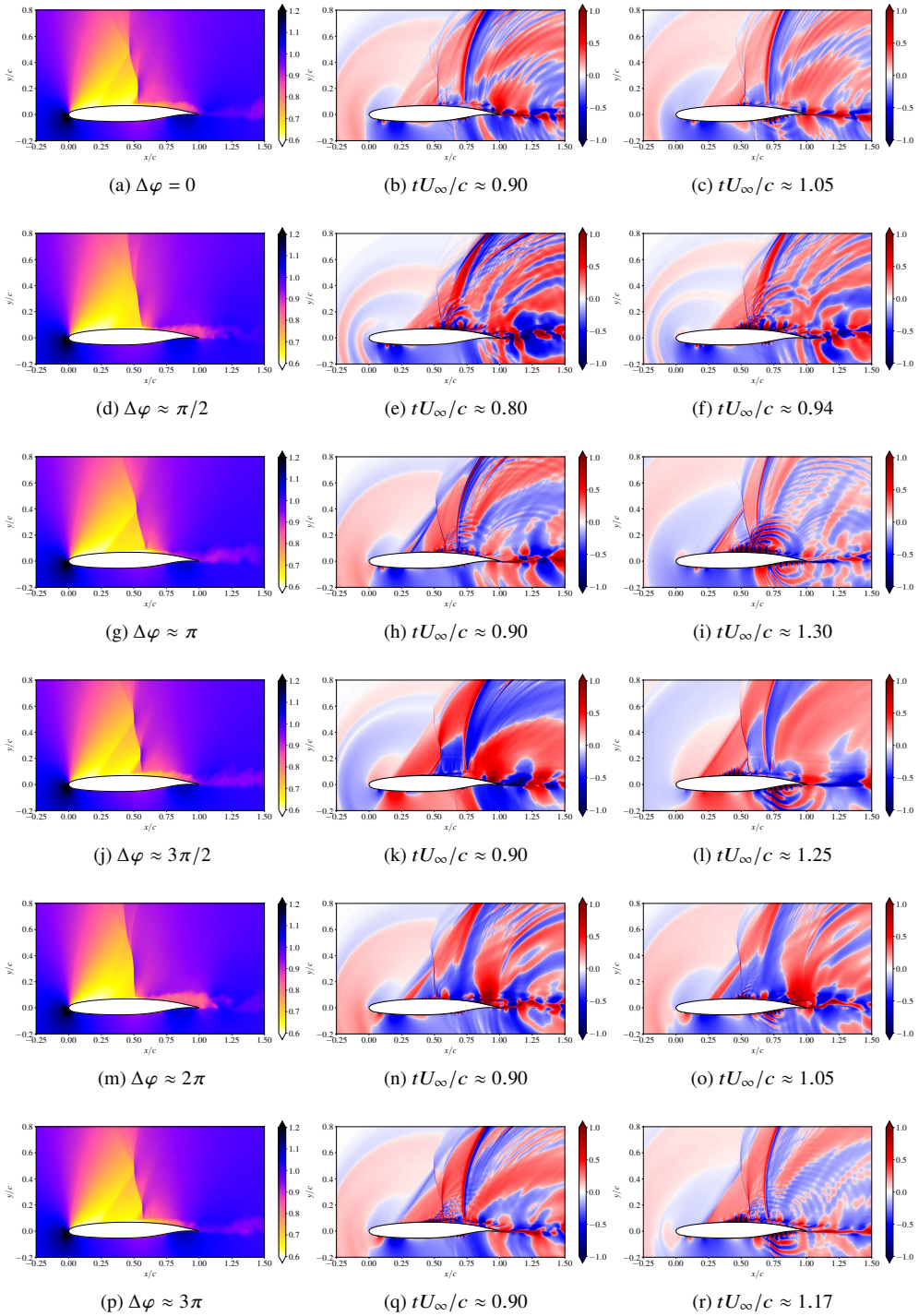

(a) $\Delta\varphi = 0$ (b) $tU_\infty/c \approx 0.90$ (c) $tU_\infty/c \approx 1.05$

(d) $\Delta\varphi \approx \pi/2$ (e) $tU_\infty/c \approx 0.80$ (f) $tU_\infty/c \approx 0.94$

(g) $\Delta\varphi \approx \pi$ (h) $tU_\infty/c \approx 0.90$ (i) $tU_\infty/c \approx 1.30$

(j) $\Delta\varphi \approx 3\pi/2$ (k) $tU_\infty/c \approx 0.90$ (l) $tU_\infty/c \approx 1.25$

(m) $\Delta\varphi \approx 2\pi$ (n) $tU_\infty/c \approx 0.90$ (o) $tU_\infty/c \approx 1.05$

(p) $\Delta\varphi \approx 3\pi$ (q) $tU_\infty/c \approx 0.90$ (r) $tU_\infty/c \approx 1.17$

Fig. 14 Visualizations of 2D base-state and perturbation density fields. The sub-figures in the first column are visualizations of the density fields in the frozen base states for different computations of the linear response. The sub-figures in other columns are visualizations of perturbation fields in each case at different times. The sub-figures in the same row correspond to the same computation with respect to the base states shown in the first column. The density fluctuations are visualized as $\left(\rho'/\rho'_{\mathrm{ref}}\right)^{1/3}$ for all cases. The evaluation of $\Delta\varphi$ corresponds to the shock buffet frequency.

Downloaded by Stanford University on January 29, 2025 | http://arc.aiaa.org | DOI: 10.2514/6.2025-2185

frozen base state can effectively reduce the fluctuations in the high-frequency regime. Accordingly, it is expected that the analysis using a frozen base state will better highlight the flow structures and mechanisms in the low-frequency regime.

In this work, six base states are selected corresponding to the computational time in the LES at 217.416 CTUs, 219.808 CTUs, 222.199 CTUs, 224.591 CTUs, 226.982 CTUs, and 231.765 CTUs. Corresponding to the shock buffet frequency, at the Strouhal number $\mathrm{St}_1 \approx 0.105$, the phase angles, $\Delta\varphi(tU_\infty/c, \mathrm{St}_1)$, relative to the first base state are 0 (by definition), and approximately $\pi/2$, π, $3\pi/2$, 2π, and 3π. The times corresponding to the selected base states are marked on the x–t diagram of the skin-friction coefficient, C_f, shown in Fig. 12. For each case, the evolution of the perturbation energy characterized by the relative Chu norm, $E_{\mathrm{Chu}}(t)/E_{\mathrm{Chu}}(t_{\mathrm{ref}})$, is shown in Fig. 13a, where t_{ref} is the same as shown in Sec. IV.A. The curves in Fig. 13a show a relatively similar linear growth for $tU_\infty/c < 1$. Compared to the growth with respect to the result obtained with the concurrently-evolving base state, the initial adjustment for all cases take approximately twice as long, and the growth is significantly slower. The measurement of the growth rates are shown in Fig. 13b. This is due to the effects of using the frozen base states, and fast evolving flow features are less resolved compared to the slowly varying flow features. When $tU_\infty/c > 1$, the curves in Fig. 13a begin to diverge. The solution shows the impact of $\Delta\phi$ that defines the base state on the linear response of the dynamic system. Nonetheless, qualitatively, the curves still have similar behavior. The growth rate after the initial linear growth begins to increase. The visualizations of the base state density and density fluctuation at different times are shown in Fig. 14. At a large scale, the perturbation flow structures are consistent with those obtained from the simulation of the linearized system with a concurrently-evolving base state. Additionally, the simulation results corresponding to the frozen base states emphasize the role of the laminar and transitioning boundary layer on the suction side of the airfoil, and provide a view of Mach wave generation in the pre-shock region due to the spatial growth of the Kelvin–Helmholtz instability.

Downloaded by Stanford University on January 29, 2025 | http://arc.aiaa.org | DOI: 10.2514/6.2025-2185

V. Conclusions

The transonic laminar shock buffet on the OALT25 airfoil is investigated based on the data of a wall-resolved LES. The LES is conducted at a freestream Mach number of 0.735. The angle of attack is 4°. The chord-length-based Reynolds number is 1×10^6. The Chu norm is used to conduct both the SPOD analysis and to indicate the amplitude of linear response in the transonic laminar shock buffet system. The SPOD is conducted to investigate the space–time correlation during shock buffet at the statistically stationary state. The linear response of the dynamic system is numerically studied by solving the linearized LES system. Both the concurrently-evolving LES solution and spanwise-averaged LES solution that is frozen in time are used as the base states. The initial perturbation of the linearized system is induced by a 2D localized impulsive pseudo body force located slightly above the turbulent boundary layer near the TE on the suction side of the airfoil.

The SPOD analysis identifies three major feedback paths. Among them, the one on the suction side of the airfoil that allows for fluctuations in the post-shock region to travel upstream bypassing the main shock within the boundary layer below the shock foot is considered to play an important role contributing to the self-sustained shock buffet. The solutions of the linearized system support the observation of the feedback mechanism. Corresponding to the initial perturbation in the post-shock region, the disturbances first travel to the pre-shock region within the boundary layer. The upstream travel of the disturbances is associated with the boundary layer breathing and/or the formation of turbulent vortex shedding. The disturbances within the pre-shock boundary layer can enter the freestream via the oscillations of the oblique shock and the Mach waves associated with the unsteadiness of the laminar separation point and transitioning to turbulence, respectively. Both the oblique shock and Mach waves carry the post-shock fluctuations and directly interact with the main shock.

Acknowledgments

This research is supported by the NASA grant / Co-operative agreement (No. 80NSSC22M0108). This research is also partially supported by the National Science Foundation (Grant No. NSF-OAC-2103509). The large-scale simulations and data processing are supported by the SummitPLUS allocation granted by the Oak Ridge Leadership Computing Facility at the Oak Ridge National Laboratory. H.S. is supported by the postdoctoral fellowship at the Center for Turbulence Research at Stanford University. The OALT25 airfoil geometry is provided by ONERA. The authors are grateful to Dr. Brion Vincent for the help in accessing the original OALT25 airfoil profile. The authors are also appreciative of Dr. Aditya S. Ghate and Dr. Markus Zauner for the helpful discussions.

References

[1] Lee, B., "Self-sustained shock oscillations on airfoils at transonic speeds," *Progress in Aerospace Sciences*, Vol. 37, No. 2, 2001, pp. 147–196.

[2] Giannelis, N. F., Vio, G. A., and Levinski, O., "A review of recent developments in the understanding of transonic shock buffet," *Progress in Aerospace Sciences*, Vol. 92, 2017, pp. 39–84.

[3] Placek, R., and Miller, M., "Wind Tunnel Tests of Laminar–Turbulent Transition Influence on Basic Aerodynamic Characteristics of Laminar Airfoil in Transonic Flow Regime," *Inst. of Aviation TR D-5.2*, Vol. 2, 2016.

[4] Placek, R., and Ruchała, P., "The flow separation development analysis in subsonic and transonic flow regime of the laminar airfoil," *Transportation Research Procedia*, Vol. 29, 2018, pp. 323–329.

[5] Jacquin, L., Molton, P., Deck, S., Maury, B., and Soulevant, D., "Experimental study of shock oscillation over a transonic supercritical profile," *AIAA Journal*, Vol. 47, No. 9, 2009, pp. 1985–1994.

[6] Masini, L., Timme, S., and Peace, A., "Analysis of a civil aircraft wing transonic shock buffet experiment," *Journal of Fluid Mechanics*, Vol. 884, 2020, p. A1.

[7] Iwatani, Y., Asada, H., Yeh, C.-A., Taira, K., and Kawai, S., "Identifying the Self-Sustaining Mechanisms of Transonic Airfoil Buffet with Resolvent Analysis," *AIAA Journal*, 2023, pp. 1–12.

[8] Balakumar, P., Iyer, P. S., and Malik, M. R., "Turbulence Simulations of Transonic Flows over an NACA-0012 Airfoil," *AIAA SciTech 2023 Forum*, 2023.

[9] Brunet, V., "Computational study of buffet phenomenon with unsteady RANS equations," *21st AIAA Applied Aerodynamics Conference*, 2003, p. 3679.

[10] Zangeneh, R., "Parametric study of separation and reattachment in transonic airfoil flows," *AIAA Journal*, Vol. 59, No. 11, 2021, pp. 4465–4474.

[11] Moise, P., Zauner, M., and Sandham, N. D., "Connecting transonic buffet with incompressible low-frequency oscillations on aerofoils," *Journal of Fluid Mechanics*, Vol. 981, 2024, p. A23.

[12] Benoit, B., and Legrain, I., "Buffeting prediction for transport aircraft applications based on unsteady pressure measurements," *5th Applied Aerodynamics Conference*, 1987, p. 2356.

[13] McDevitt, J. B., and Okuno, A. F., "Static and dynamic pressure measurements on a NACA 0012 airfoil in the Ames high Reynolds number facility," Tech. rep., 1985.

[14] Iovnovich, M., and Raveh, D. E., "Reynolds-averaged Navier-Stokes study of the shock-buffet instability mechanism," *AIAA Journal*, Vol. 50, No. 4, 2012, pp. 880–890.

[15] Fukushima, Y., and Kawai, S., "Wall-modeled large-eddy simulation of transonic airfoil buffet at high Reynolds number," *AIAA Journal*, Vol. 56, No. 6, 2018, pp. 2372–2388.

[16] Deck, S., "Numerical simulation of transonic buffet over a supercritical airfoil," *AIAA Journal*, Vol. 43, No. 7, 2005, pp. 1556–1566.

[17] Grossi, F., Braza, M., and Hoarau, Y., "Prediction of transonic buffet by delayed detached-eddy simulation," *AIAA Journal*, Vol. 52, No. 10, 2014, pp. 2300–2312.

[18] Lee, B., "Oscillatory shock motion caused by transonic shock boundary-layer interaction," *AIAA Journal*, Vol. 28, No. 5, 1990, pp. 942–944.

[19] Crouch, J., Garbaruk, A., and Magidov, D., "Predicting the onset of flow unsteadiness based on global instability," *Journal of Computational Physics*, Vol. 224, No. 2, 2007, pp. 924–940.

[20] Taira, K., Brunton, S. L., Dawson, S. T., Rowley, C. W., Colonius, T., McKeon, B. J., Schmidt, O. T., Gordeyev, S., Theofilis, V., and Ukeiley, L. S., "Modal analysis of fluid flows: An overview," *AIAA Journal*, Vol. 55, No. 12, 2017, pp. 4013–4041.

[21] Gur, O., Schetz, J. A., and Mason, W. H., "Aerodynamic considerations in the design of truss-braced-wing aircraft," *Journal of Aircraft*, Vol. 48, No. 3, 2011, pp. 919–939.

Downloaded by Stanford University on January 29, 2025 | http://arc.aiaa.org | DOI: 10.2514/6.2025-2185

[22] Brion, V., Dandois, J., Abart, J.-C., and Paillart, P., "Experimental analysis of the shock dynamics on a transonic laminar airfoil," *Progress in Flight Physics–Volume 9*, Vol. 9, 2017, pp. 365–386.

[23] Dandois, J., Mary, I., and Brion, V., "Large-eddy simulation of laminar transonic buffet," *Journal of Fluid Mechanics*, Vol. 850, 2018, pp. 156–178.

[24] Zauner, M., and Sandham, N. D., "Modal analysis of a laminar-flow airfoil under buffet conditions at Re= 500,000," *Flow, Turbulence and Combustion*, Vol. 104, No. 2, 2020, pp. 509–532.

[25] Zauner, M., Moise, P., and Sandham, N. D., "On the co-existence of transonic buffet and separation-bubble modes for the OALT25 laminar-flow wing section," *Flow, Turbulence and Combustion*, Vol. 110, No. 4, 2023, pp. 1023–1057.

[26] Towne, A., Schmidt, O. T., and Colonius, T., "Spectral proper orthogonal decomposition and its relationship to dynamic mode decomposition and resolvent analysis," *Journal of Fluid Mechanics*, Vol. 847, 2018, pp. 821–867.

[27] Song, H., Wong, M. L., Ghate, A. S., and Lele, S. K., "Numerical study of transonic laminar shock buffet on the OALT25 airfoil," *AIAA SciTech 2024 Forum*, 2024.

[28] Vreman, A., "An eddy-viscosity subgrid-scale model for turbulent shear flow: Algebraic theory and applications," *Physics of Fluids*, Vol. 16, No. 10, 2004, pp. 3670–3681.

[29] Lele, S. K., "Compact finite difference schemes with spectral-like resolution," *Journal of Computational Physics*, Vol. 103, No. 1, 1992, pp. 16–42.

[30] Castro, M., Costa, B., and Don, W. S., "High order weighted essentially non-oscillatory WENO-Z schemes for hyperbolic conservation laws," *Journal of Computational Physics*, Vol. 230, No. 5, 2011, pp. 1766–1792.

[31] Wong, M. L., and Lele, S. K., "High-order localized dissipation weighted compact nonlinear scheme for shock-and interface-capturing in compressible flows," *Journal of Computational Physics*, Vol. 339, 2017, pp. 179–209.

[32] Song, H., Ghate, A. S., Matsuno, K., West, J., Subramaniam, A., Brown, L. J., and Lele, S. K., "Robust high-resolution simulations of compressible turbulent flows without filtering," *AIAA Aviation 2022 Forum*, 2022.

[33] Song, H., Ghate, A. S., Matsuno, K. V., West, J. R., Subramaniam, A., and Lele, S. K., "A robust compact finite difference framework for simulations of compressible turbulent flows," *Journal of Computational Physics*, Vol. 519, 2024, p. 113419.

[34] Song, H., Matsuno, K. V., West, J. R., Subramaniam, A., Ghate, A. S., and Lele, S. K., "Scalable parallel linear solver for compact banded systems on heterogeneous architectures," *Journal of Computational Physics*, Vol. 468, 2022, p. 111443.

[35] Welch, P., "The use of fast Fourier transform for the estimation of power spectra: a method based on time averaging over short, modified periodograms," *IEEE Transactions on audio and electroacoustics*, Vol. 15, No. 2, 1967, pp. 70–73.

[36] Schmidt, O. T., and Colonius, T., "Guide to spectral proper orthogonal decomposition," *AIAA Journal*, Vol. 58, No. 3, 2020, pp. 1023–1033.

[37] Chu, B.-T., "On the energy transfer to small disturbances in fluid flow (Part I)," *Acta Mechanica*, Vol. 1, No. 3, 1965, pp. 215–234.

Downloaded by Stanford University on January 29, 2025 | http://arc.aiaa.org | DOI: 10.2514/6.2025-2185